The granular jump

By J. F. BOUDET, Y. AMAROUCHENE,
B. BONNIER AND H. KELLAY

Centre de Physique Moléculaire Optique et Hertzienne, UMR 5798, Université Bordeaux 1,
351 cours de la Libération, 33405 Talence, France

When a fluid jet hits a solid surface, a hydraulic jumps occurs. This jump sharply delimits a thin film of liquid from a thicker film. We show here that a granular jet impinging on a solid surface also gives rise to several features reminiscent of the hydraulic jump and we refer to this situation as the granular jump. We describe, in detail, this phenomenon and show that if many of its features can be understood in analogy with the hydraulic jump, others are directly related to the granular nature of the medium and, in particular, the small-scale dynamics of the jump.

1. Introduction

Granular materials exhibit behaviour that crosses the frontiers between different states of matter. They can behave as liquid, solid or gas (Nagel 1992; Jaeger 1996; de Gennes 1999; Kadanoff 1999). In certain situations, driven granular materials show features reminiscent of instabilities seen for fluids such as the Faraday instability, the occurrence of Taylor vortices, or the Kelvin–Helmholtz instability (Melo, Umbanhowar & Swinney 1995; Garcimartin *et al.* 2002; Goldfarb, Glasser & Shinbrot 2002; Conway, Shinbrot & Glasser 2004). In other situations, differences with fluids arise immediately such as the flow of sand around an obstacle, or the formation of arches and the ability to jam and form clusters (Liu & Nagel 1998; Amarouchene, Boudet & Kellay 2001; Rericha *et al.* 2002; Zuriguel *et al.* 2005). The study of the analogies and differences between liquid behaviour and granular flows is therefore important for the understanding of the subtle properties of granular flows.

In this respect, work on the description of rapid granular surface flows using depth-averaged equations and its relations to the so-called shallow-water equations has been instructive. Savage & Hutter (1989) considered this problem in relation to the spreading of avalanches. The small thickness of the flow considered allows an integration over the thickness to obtain one-dimensional equations for the average thickness of the avalanche and its velocity. Subsequent studies by several authors have applied the Savage & Hutter model to the understanding of avalanches and ways to divert them. Gray, Tai & Noelle (2003) showed that the hydraulic model is sufficient to capture several qualitative features and that bores and oblique shocks, obtained experimentally, can be understood within this formalism. Hákonardóttir & Hogg (2005) showed, through systematic measurements on oblique shocks, that the shallow-water equations, with slight modifications, are adequate for describing their experimental observations. Such depth-averaged models can be extended to take more complicated friction laws into account (Pouliquen & Forterre 2002).

In this work, we consider a situation equivalent to the circular hydraulic jump which arises when a vertical jet of liquid impinges continuously on a rigid planar surface

normal to the jet axis (Watson 1964; Bush & Aristoff 2003). This impact gives rise to a radial horizontal flow which consists of two regions: near the jet axis, the flow is rapid and the liquid film is thin, but at some distance from the impact point there is a narrow annular region, known as the jump, over which the film thickness suddenly increases. Beyond this jump, the thick liquid layer moves at a slower speed than the thin film. Various phases (the falling jet, the thin and thick layers separated by the jump) are involved in the hydraulic jump. Our aim here is to describe the behaviour of a granular flow in analogous circumstances. We show that several features of the obtained patterns are similar to those obtained with simple liquids whereas other characteristics are related purely to the granular nature of the material. The example studied here extends previous work on the similarities between rapid granular flows and shallow-water flows.

2. Observation of the granular jump

We perform a set of experiments where a granular material is poured from a funnel fixed at some distance above a flat horizontal surface. We observe that when the falling column or jet of granular material impacts the surface, it fragments and gives rise to a thin and fast radial flow of grains just like the thin and fast layer for liquids. This flow then decelerates because of friction against the flat plate, and stops as a circular ring. Upon further injection of sand, this initial circular ring evolves and gives rise to a pattern whose front moves towards the injection point. Figure 1 shows an overview of this phenomenon. The circular jet in the middle impacts the flat glass plate giving rise to a thin and fast radial flow which, because of friction, stops and gives rise to a ring that closes as more sand is injected. The deposited sand which forms the outer ring in figure 1(*a*), shows circular ripples as we have previously reported (Boudet *et al.* 2005). Figure 1(*b*) shows a close-up of the impact region. The jet in the centre impacts the plate, keeping a well-defined curved shape. This impact gives rise to a horizontal layer which, as it encounters the accumulated sand, forms a jump. The position of the jump moves towards the impact region as the circular ring closes.

Figures 1(*c*), 1(*d*), and 1(*e*) show, respectively, the outer ring visualized as a radial cut using a laser sheet falling perpendicularly to the sand pile, with many well-defined ripples which are engendered by the oscillations of the jump itself (figure 1*d*, *e*). Indeed, the jump moving towards the injection point is an example of a sand front (Mahadevan & Pomeau 1999; Bonnier, Boudet & Kellay 2003; Boudet *et al.* 2003) which has an angle with the horizontal that changes as the front moves. This angle oscillates between a maximal angle (figure 1*e*) and a minimal angle (figure 1*d*) close to the repose angle. These oscillations are due to a stick–slip type of motion of the sand front and engender the oscillations of the deposited sand profile. The wavelength of these ripples has been the subject of a previous study (Boudet *et al.* 2005) where it was found to be of the order of a few millimetres and to increase linearly versus the funnel diameter or equivalently the jet diameter.

Figure 2 shows a schematic of the granular jump studied here. The granular jet in the middle has a diameter $D(z)$, where z is the vertical distance from the funnel outlet: $D(z)$ is a decreasing function of z since the jet thins as it falls. The sand layer after impact has a height denoted by $h(R)$, (R being the radial distance from the impact position), which is curved near the jet impact position, becomes small and constant, as we will see below, after impact, and then increases at the level of the jump and in the annular region beyond the jump. This annular region starts with a height denoted
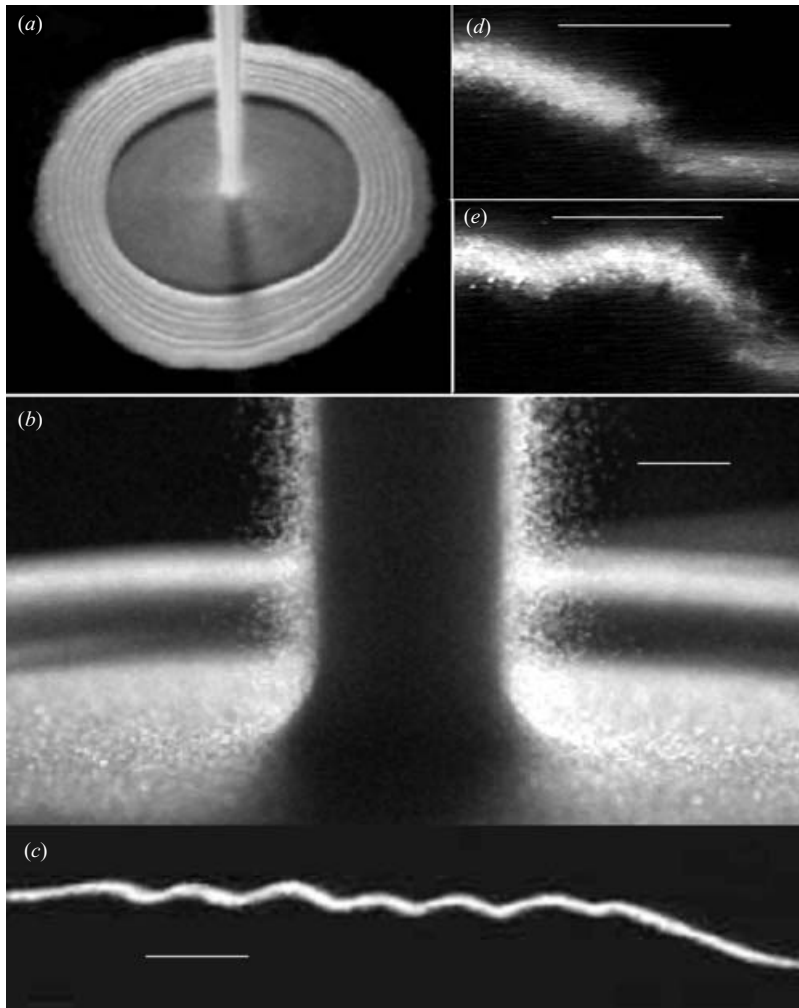
FIGURE 1. (*a*) A view from above showing the column of sand at the centre and the surrounding jump showing signs of ripples on the outer annulus. The diameter of the outer annulus is 18 cm. (*b*) An expanded view of the jet impact and the granular jump in the background. (*c*) A laser sheet falling perpendicularly to the sand pile helps to visualize the surface profile of the sand pile and the ripples. (*d*) and (*e*) An expanded view of (*c*) during the dynamic process. The ripples are formed by an oscillation of the front. In (*e*) the sand front has a high slope whereas in (*d*) the front has relaxed to a lower slope. The scale bars have a length of 0.3 cm.

h_J at $R = R_J$ and has an increasing height $h_\infty(R)$ as R decreases towards the jump position.

From its ejection up to its deposition, the granular material thus experiences several phases. We distinguish five phases which are studied in terms of three basic control parameters: the diameter d of the glass beads which compose the granular material, the diameter D of the funnel outlet, and the chute height H. We point out, in particular, the interplay between the granular-like and the fluid-like behaviour of these successive phases.

Before its arrest, we distinguish three phases in the flow: the vertically falling jet; the impact region; and the thin horizontal layer. After a transient regime, a stationary
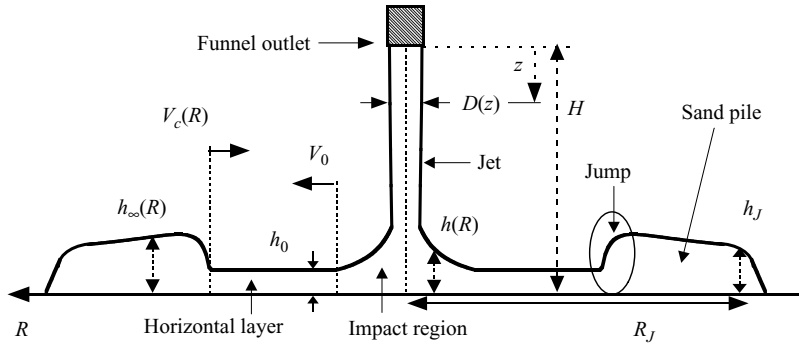
FIGURE 2. A schematic of the granular jump. z is the vertical axis (the origin is the funnel outlet and H the distance between the funnel and the horizontal surface), R the radial distance from the impact centre. The jet is characterized by its local radius $D(z)$, velocity $V(z)$ and density $\rho(z)$. After the impact, we refer to the height of the sand layer as $h(R)$ near the impact, h_0 for the horizontal layer and $h_\infty(R)$ in the sand pile, this region starts with a height h_J at $R = R_J$. V_0 is the speed in the horizontal layer near the jet impact, and $V_c(R)$ is the closing speed of the sand pile.

regime takes place. This transient regime is the result of the first impact of the jet on the solid surface. As a consequence of this transient, we distinguish two sequences in the deposition process: the granular initial jump formation and the filling phase. Roughly speaking, the granular jump is formed by the arrest of the horizontal layer during its transient, i.e. as the jet first impacts the solid surface. This arrest is due to friction effects described well by the usual Coulomb law, and during this period the deposited species reach a maximal height h_J at radial position R_J which characterize the initial jump. Then the horizontal layer reaches its stationary regime and collides with the jump previously formed whose characteristics remain, however, unchanged. This corresponds to the beginning of the filling phase where the deposited species form a sand pile moving towards the injection centre. In this phase, the incoming flow decelerates by friction, but its arrest, due to the collision with the previously accumulated grains, is more sudden as R decreases.

The filling phase appears as a succession of short periods comparable to the first one (the formation of the initial jump) with the end of each period corresponding to an instability of the advancing front. This instability appears when the slope of the advancing front exceeds some maximal slope, and a remnant of this oscillating dynamics is the presence on the whole surface of the sand pile of a regular pattern of concentric ripples with a constant wavelength λ. During the deposition, the width of the advancing front is of the order of λ, which is only a few millimetres. We can thus model the sand front dynamics at two scales: a global one where the fluctuations of order λ are neglected, and a local one with a range $\delta R = \lambda$ where the fluctuations are taken into account.

3. Experimental details

The experiments use different size funnels and different sized grains (glass beads). The impacted surface is made of smooth glass and the range of variation of the control parameters is $0.4\,\mathrm{cm} \leqslant D \leqslant 2.4\,\mathrm{cm}$ for the funnel outlet diameter, $3\,\mathrm{cm} \leqslant H \leqslant 150\,\mathrm{cm}$ for the chute height and $70\,\mu\mathrm{m} < d < 500\,\mu\mathrm{m}$ for the diameter of the glass beads which compose the granular material. An important feature of the granular jump studied

here is its height profile whether in the static sand pile, near the impact zone, or in the horizontal dilute fast-flowing layer. This profile was visualized using a thin laser sheet which falls perpendicularly to the pattern. This laser sheet is scattered by the surface of the heap, so the surface appears bright when viewed from the side. Figure 1(*c*) is an illustration of this technique for visualizing the ripple pattern, for example. A CCD camera operating both at standard rates (25 images per second) and at faster rates (between 250 and 1000 images per second) was used to record the images. For the horizontal layer, and since it is dilute, the laser sheet light is multiply scattered by the layer. This scattered light when viewed from the side, appears as a bright band. The thickness of this layer was then extracted from the profile of the band of scattered light. This profile is Gaussian-like, and its half width gives the thickness of the layer. Direct visualizations of the flowing grains were also carried out using either transmitted broad white light or illumination from above, so the granular density could be evaluated and the results could be checked. A combination of these two techniques allowed us to extract the thickness of the thin dilute horizontal layer. The velocity measurements were carried out mostly by laser-Doppler velocimetry (LDV). This technique turns out to be well adapted to granular flows as has been demonstrated by Zuriguel *et al.* (2005) and Amarouchene & Kellay (2006). The principle of this technique, which is widely used in experiments in fluid dynamics, is simple. It uses a laser beam which is split in two by a beam splitter. These two beams are then brought together with a lens to form a thin spot where the two beams interfere. As particles cross this intersection zone, they scatter the light when they cross a bright fringe. The scattered signal is therefore modulated as the particle crosses several bright fringes. An analysis of this signal allows us to extract the modulation frequency which is directly proportional to the transit velocity of the particle as it crosses the scattering volume (which is 0.1 mm in diameter). We have used a commercial laser-Doppler velocimetry (two-dimensional flowlite from Dantec dynamics) capable of measuring the velocity in two perpendicular directions as it uses two colours and four beams. The LDV velocity measurements were complemented by measurements using particle imaging velocimetry (PIV) which is now standard in measuring the velocity in granular flows.

4. The fluid phases in the stationary regime

We begin here with a description of the sand flow in its stationary regime which presents some analogy with a compressible fluid. In particular, most of its characteristics are practically independent of the diameter d of the beads in the range we consider (to be precise the given results correspond to $d = 116\,\mu\text{m}$). The only noticeable exception is the depth of the thin horizontal layer outside the impact region which appears to be a packing of a few bead layers and is thus proportional to d.

We first measured the flux of the sand coming out of the funnel used to pour the sand as a column. The measured injected mass flux Q varies with the funnel diameter D according to the usual law $Q \propto D^{5/2}$ and it is given

$$Q = 0.29\pi\rho_c\sqrt{g}D^{5/2}, \tag{4.1}$$

where ρ_c is the compact density of the granular material ($\rho_c = 1.44\,\text{g cm}^{-3}$) and g the standard gravity constant. The speed of the flow when it leaves the funnel outlet is thus $V(0) = 4Q/\pi\rho_c D^2 = 1.16\sqrt{gD}$. This velocity corresponds to a fall inside the funnel of a vertical distance of order D under an effective acceleration $ge^{-\chi} = 0.68g$,
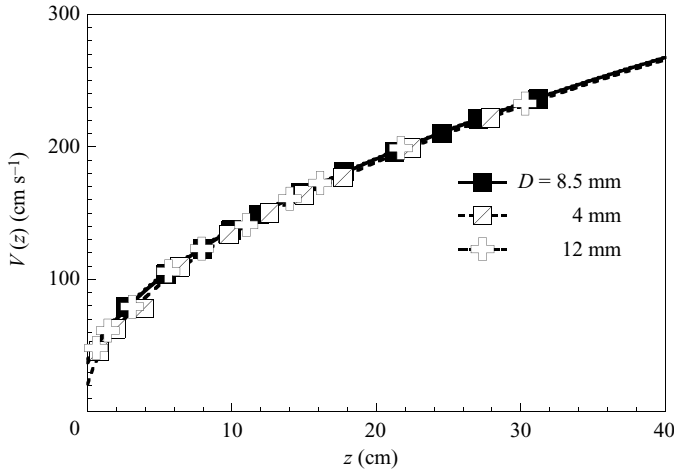
FIGURE 3. The vertical speed $V(z)$ as function of z the distance from the funnel outlet. The lines are fits using (4.2). $g' = 877\,\mathrm{cm\,s^{-2}}$; $d = 116\,\mu\mathrm{m}$.

where the decompaction factor χ, introduced into the dynamic Janssen effect (Duran 1997), has in our case the value $\chi \approx 0.4$.

All the phases appearing in the course of the experiment have rotational symmetry around the vertical axis Oz of the falling jet ($z = 0$ and $z = H$ correspond to the funnel outlet and to the impact point, respectively), and in the following we describe a radial section of the flow.

4.1. *The vertical jet*

We began by characterizing the falling jet through measurements of the speed of fall versus the height z, the diameter of the jet and consequently, the density of the falling jet.

The measurements of the vertical speed $V(z)$ of the jet at various distances z from the funnel outlet, using laser Doppler velocimetry, are shown in figure 3 and indicate that the chute appears as a free fall under an effective gravity g', as usually observed in granular chute flow (Duran 1997), independent of D, i.e.

$$V(z) = \sqrt{2g'z + V^2(0)} \qquad (g' \approx 877\,\mathrm{cm\,s^{-2}}). \tag{4.2}$$

The diameter $D(z)$ of the jet decreases during the fall, as the jet thins, and the various data for different funnel diameters are shown in figure 4. These data can be reduced to the form

$$\frac{D(z)}{D} \sim \left(\frac{z}{D}\right)^{-1/6}, \tag{4.3}$$

where the exponent $-1/6$ is the best fit, as shown in figure 4. This exponent is not far from the value $-1/4$ given in the case of liquids and is due to mass conservation (Middleman 1995). Figure 4 shows that the shape of the jet is universal once $D(z)$ and z itself are rescaled by the funnel diameter. This scaling is valid for distances z greater than D. The density $\rho(z)$ of the jet is then given by the mass conservation relation $Q = \pi \rho(z) D(z)^2 V(z)/4$ and is found to decrease during the fall according to:

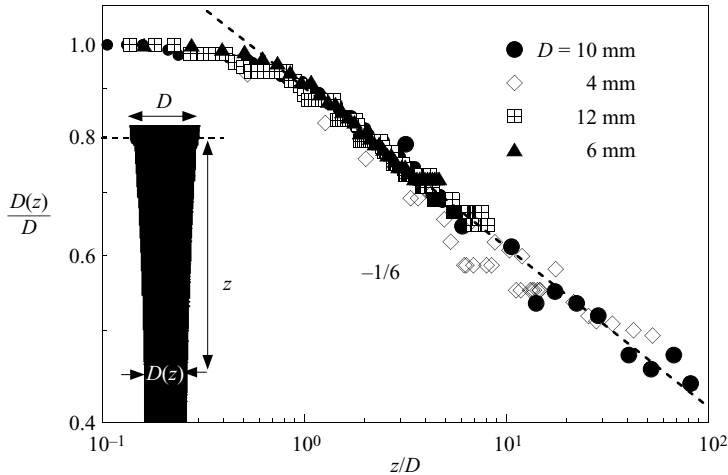$$\rho(z) \sim \left(\frac{z}{D}\right)^{-1/6}. \tag{4.4}$$

FIGURE 4. The diameter of the jet $D(z)$ normalized by D as a function of z/D for several funnel diameters ($d = 116\,\mu m$). The inset shows a photograph of the jet.

This expression is valid when the chute height is greater than about two funnel diameters. On the other hand, for important chute heights, the jet becomes unstable and breaks into droplet-like structures. This instability, which completely destroys the jet, appears for $z_c \approx$ 20, 40, 100, 140 cm for $D =$ 0.4, 0.6, 1, 1.2 cm, respectively (the jet density is then $0.4\rho_c$ approximately). Between these two limiting values, the expressions (4.2), (4.3) and (4.4) describe the stationary regime of a stable granular jet, where the collective motion of the grains allows them to penetrate the air more easily than isolated ones. These collective effects are probably also present in the case of gravity-driven dense suspension jets (Nicolas 2002), where, before the appearance of instabilities, the suspension falls like a solid body.

The experiments analysed in this work are performed with stable jets. When the jet reaches its limit of stability, the dynamics of the flow is very different from the behaviour depicted in the following sections. In particular, the granular deposition is no longer made on a small range and involves particles going way beyond the jump. As a result, the observed shape of the sand pile and its dynamics are different from the one described here, and the regular ripples disappear in experiments at large fall heights.

4.2. *The impact region*

In the stationary regime, the transition from vertical to horizontal motion occurs in a region which can be accurately delimited by inspection of the surface profile. The appearance of the surface in this region is smooth, comparable with the surface profile of the falling jet, suggesting that the grains follow curved trajectories (see figure 1*b*) driven by some underlying accumulation of quasi-static grains. Indeed, a camera placed below the impacted surface in the jet axis shows slow motion of the grains in a radius of the order of $D(H)$.

The surface profile in the impact region was obtained using video imaging of a laser sheet falling perpendicularly to the jet since the surface of the jet and of the impact region scatter light strongly. This profile denoted $h(R)$ is small far from the impact point and increases rapidly as the jet is approached. We characterize the impact region in the following way. When the radial distance R corresponds to the radius of the vertical jet ($R \approx D(H)/2$), the surface profile begins to bend from the vertical position
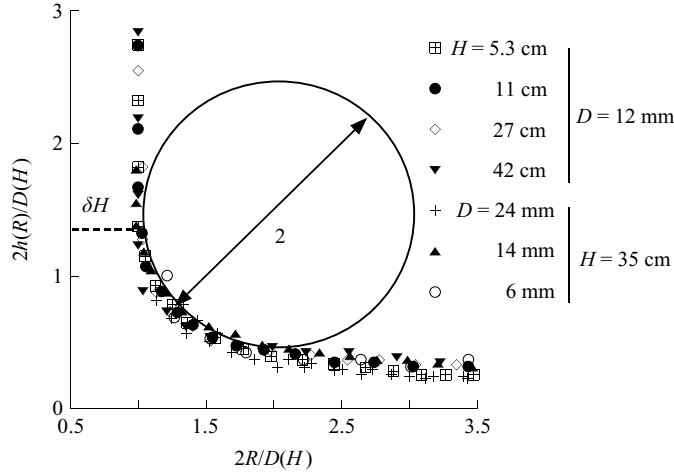
FIGURE 5. The height profile $h(r)$ in the impact region as a function of the radial distance R for several funnel diameters and chute heights. The scales are normalized by the jet radius before the impact $D(H)/2$.

defined by the falling jet (it starts to bend at a height δH of a few millimetres) into a smooth curved profile which becomes nearly horizontal for R greater than a distance R_0 with a height h_0 (h_0 is less than 1 mm as we will see below). At radial distances greater than R_0, the flow remains horizontal with a velocity profile practically flat as described below. The impact region thus extends for $0 \leqslant R \leqslant R_0$ and is limited for $R \geqslant D(H)/2$ by a smooth profile whose minimal radius of curvature appears to be given approximately by $D(H)/2$. This is shown in figure 5 where it is also shown how various profiles of the impact zone can be rescaled onto a single one. Both $h(R)$ and R are rescaled by the diameter of the jet at the fall height H. The shape of the jet versus the chute height as well as the shape of the impact region of the jet with the surface turn out to be universal after a simple rescaling by the diameter of the jet.

The properties of the jet, $\rho(H)$, $V(H)$ and $D(H)$, as it enters the impact region are known as shown above (δH can be neglected). The flow then exits this region at R_0 with velocity V_0 and occurs in a horizontal thin layer with height h_0. The three quantities can be measured separately. As the mass conservation in the radial section reads $R_0 h_0 V_0 \rho(R_0) = Q/2\pi$, the density $\rho(R_0)$ can be deduced from these measurements, with the result that it is close to the compact density ρ_c. From measurements of V_0 versus H we have evidenced the following conservation law for the transition from vertical to horizontal flow:

$$\rho(H)V(H) = \rho_c V_0, \tag{4.5}$$

which implies, through mass conservation, the relation $R_0 = D^2(H)/8h_0$ which gives the extent of the impact region and therefore the location of the transition from vertical flow to horizontal flow. The validity of these expressions has been systematically checked and we give, for example, in figure 6 the measured values of V_0 compared to their values given by $V_0 = \rho(H)V(H)/\rho_c = 4Q/\pi\rho_C D^2(H)$ according to (4.5); the agreement is very good. In terms of the control parameters, this relation is

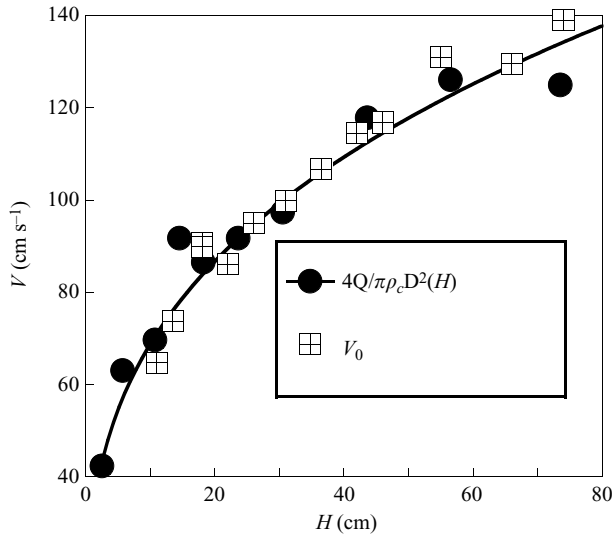$$V_0 \approx 1.4 \sqrt{g} H^{1/3} D^{1/6}. \tag{4.6}$$

FIGURE 6. The speed V_0 measured with the LDV at $R = R_0$ as a function of the chute height (squares). The circles show the values of the speed deduced from the measured jet diameter. The line is the result of (4.6).

The relative energy lost in the impact region is thus important, since the square root of the restitution coefficient $e^{1/2} = V_0/V(H) = 1.05(D/H)^{1/6}$ varies between 0.5 and 0.8. These values are not far from those obtained by Staron & Hinch (2005), albeit in a different configuration.

In spite of the typical effects due to the compressibility of the granular flow at impact, its smooth transition from vertical to horizontal motion offers some similarities with a hydrodynamic flow. In particular, the conservation relation (4.5), implies that the density and the speed after impact are determined solely by the properties of the falling jet.

4.3. *The horizontal layer*

The horizontal layer corresponds, in a radial cut, to the moving species in the region $R \geqslant R_0$, with an initial height h_0 and speed V_0, the density being near the compact density at R_0. In the stationary regime, this flow begins as a supersonic shallow layer (Amarouchene & Kellay 2006), slows down by friction with the horizontal surface as it propagates, then collides with the sand front or jump which moves in the opposite direction. This process results, by deposition, in an increase in the size of the sand pile. Before this collision, the characterization of the layer is simple. Its depth h_0 is small and constant during the propagation. This height was determined from the multiple scattering of the laser light sheet. A snapshot of this scattering pattern is shown in figure 7 where it appears as a bright band. A cut at a particular location R shows a Gaussian-like profile. A slight asymmetry can be seen in the experimental profile, however. We have identified the half-width of this profile as the thickness of this layer. Confirmation of this procedure for the measurement of this thickness comes from direct visualizations of this flow and from the matching with the previously determined profile near the impact region, which is simpler to extract from the surface scattering of the laser light as explained above. This value, independent of the chute height and of the funnel diameter, is linear versus the diameter of the
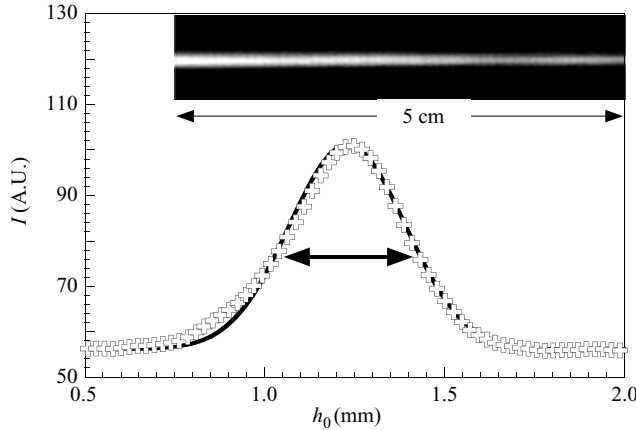
FIGURE 7. The photograph shows the light scattering of the laser sheet by the horizontal layer. Notice that the intensity of the scattered light decreases from left to right. The flow here is from left to right. The intensity decreases since the density of the horizontal layer decreases with the distance from the impact point. The figure shows a vertical cut at one location R of the light intensity scattered by the horizontal layer (circles) and the curve is fit to a Gaussian profile, the half-width of which determines the thickness h_0 at that location.
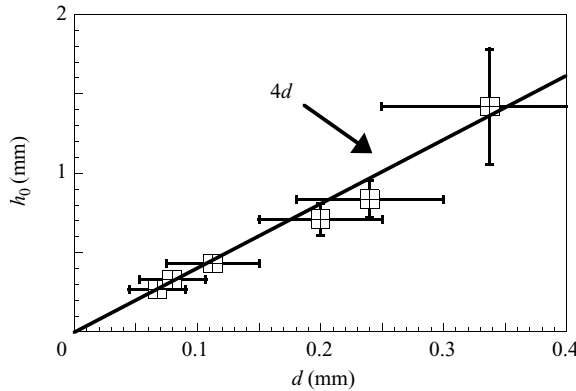

FIGURE 8. The horizontal layer thickness as a function of the bead diameter d. The straight line is equal to $4d$.

beads (figure 8). We find that $h_0 \sim 4d$. This height h_0 changes when the nature of the surface changes and was found to be greater for rougher surfaces.

As R increases, the speed of the particles in the horizontal layer $V_0(R)$ decreases according to the Coulomb law which predicts an arrest point at $R = R_M = R_0 + V_0^2/2\mu g \approx V_0^2/2\mu g$. Thus, from (4.6) for V_0

$$R_M \approx 1.6 H^{2/3} D^{1/3}, \qquad V_0(R) \approx V_0 \sqrt{\left(1 - \frac{R}{R_M}\right)}. \tag{4.7}$$

From the mass conservation relation, the density, which behaves as $R^{-1}(1 - R/R_M)^{-1/2}$, strongly decreases as R increases. A plot of $V_0(R)$ determined using the LDV and PIV techniques is shown in figure 9 along with a fit to the above equation using $\mu \approx 0.6$. The agreement is good, giving the value of the dynamic friction coefficient of the
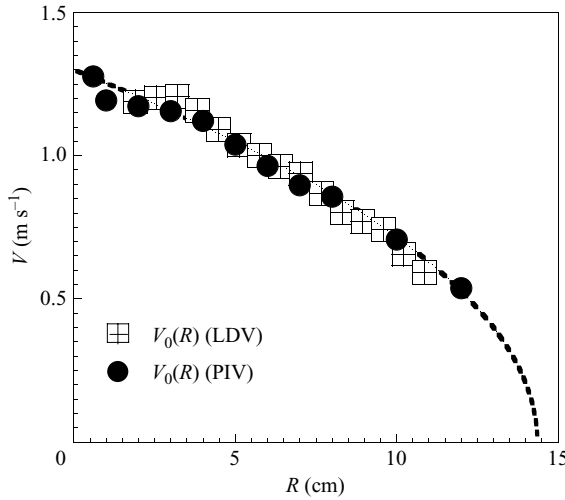
FIGURE 9. The velocity of the horizontal layer versus the radial distance from the impact point. The line is a fit using the expression given in the text (equation (4.7)) giving a dynamic friction coefficient of 0.6.
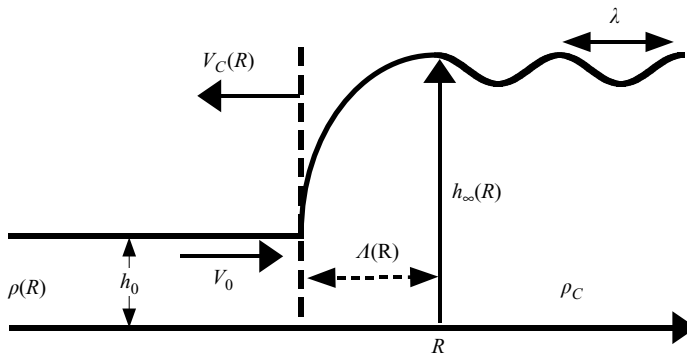

FIGURE 10. A schematic of the granular jump with the different length scales.

horizontal layer against the glass plate. The coefficient 1.6 in (4.7) for R_M is obtained assuming the measured value of $\mu = 0.6$.

5. The filling phase

In order to complete our preliminary results (Boudet *et al.* 2005) we give, here, a detailed description of the sand front dynamics. A basic property of the observed front is its small spatial extension (in a radial cut) which can be characterized by a width Λ which is time-dependent, but always of the order of the ripple wavelength λ. We define Λ in the following way: if, at time T, the summit of the front is located at some radial position R, then its base is at position $R - \Lambda$ (see figure 10). Thus, at any time, we can distinguish on the profile a dynamic front (which moves towards the origin with a mean horizontal speed $V_c(R)$) and a final profile $h_\infty(R)$ extending from R to R_J. A striking feature of $h_\infty(R)$ is the presence of small and quasi-periodic fluctuations around a mean profile $h_c(R)$. This reflects the presence of the ripples

already mentioned and can be expressed through the relations

$$h_\infty(R) = h_c(R)(1 + \varepsilon(R)), \qquad h_c(R) = q/RV_c(R), \qquad q = Q/2\pi\rho_c, \qquad (5.1)$$

where the fluctuation $\varepsilon(R)$ of maximal amplitude of the order of ± 0.1 has a period λ. In (5.1), the second equality comes from the radial mass conservation relation for the mean values.

Since λ and Λ are small lengths of 2–4 mm (Boudet *et al.* 2005), we can split the study of the dynamics into two steps: a global analysis where the fluctuations are neglected ($\lambda = \Lambda = \epsilon = 0$) and a small scale analysis where the fluctuations are taken into account perturbatively.

For the large-scale analysis, the results of the following paragraph show that a description borrowed directly from the hydraulic jump determination gives an acceptable determination of the mean profile $h_c(R)$ and closure speed $V_c(R)$.

For the dynamics of the front at the wavelength scale λ, we must consider the advent of avalanches to explain its local speed and slope fluctuations and the granular effects become dominant as we have shown previously (Boudet *et al.* 2005).

5.1. *Determination of the final profile and of the closing speed*

At large scales, the sand-pile formation at radial position R appears as a vertical jump suddenly formed by a granular flow which encounters the following discontinuities: for $R = R^-$, the characteristics of the flow $\rho(R)$, $V_0(R)$, h_0 are those of the horizontal incoming flow in its stationary regime, given in §4, and for $R = R^+$, the characteristics of the flow are those of the sand pile ρ_c, $V_c(R)$, $h_c(R)$.

The mass conservation reads $h_0\rho(R)(V_0(R) + V_c(R)) = \rho_c V_c(R)h_c(R) = Q/2\pi R$ and the momentum conservation requires that the difference in pressure forces across the jump balance the difference in radial momentum flux as in the hydraulic jump (Middleman 1995), i.e.

$$h_0\rho(R)V_0(R)(V_0(R) + V_c(R)) = \tfrac{1}{2}g\left(\rho_c h_c(R)^2 - \rho(R)h_0^2\right). \qquad (5.2)$$

Here, we used an expression for the pressure (on the right-hand side) identical to that used in the case of a hydraulic jump, i.e. the hydrostatic pressure as proposed since Savage & Hutter's work (Savage & Hutter 1989; Pouliquen & Forterre 2002; Gray *et al.* 2003; Hákonardóttir & Hogg 2005). Since $V_0(R)$ is large compared to $V_c(R)$ and h_0 small compared to $h_c(R)$, we retain the leading terms in this expression and obtain:

$$h_c(R) \approx \sqrt{QV_0(R)/\pi g\rho_c R}, \qquad (5.3)$$

$$V_c(R) \approx \tfrac{1}{2}\sqrt{g\,Q/\pi\rho_c RV_0(R)}. \qquad (5.4)$$

Figure 11 shows the measured mean profile $h_c(R)$. The height of the sand pile left behind the front increases as the impact point is approached. The dependence of this profile on the distance R turns out to be approximated well by the expression above where all the terms are known. This figure illustrates the central result of this paper, namely that the profile of the deposited sand can be understood using a balance between the momentum flux across the jump and the hydrostatic pressure difference.

Such comments can be transposed to the closing speed, since it is simply derived from the profile through mass conservation. Equation (5.4) gives the correct dependence of the closing speed versus the radial distance R as shown by the solid line in figure 12. Again, all the terms in the expression for the closing speed are known. These data show that the speed increases rapidly as the front reaches the impact point. This is another important aspect of this study illustrating that the jump
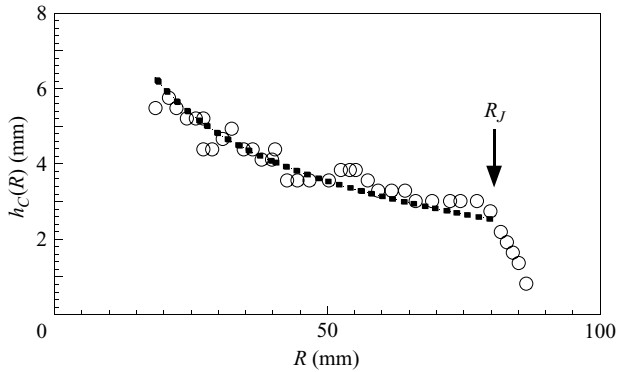
FIGURE 11. A typical profile $h_c(R)$ for $H = 20$ cm, $D = 12$ mm, and $d = 160$ μm. The solid line is the result of (5.3) given in the text.
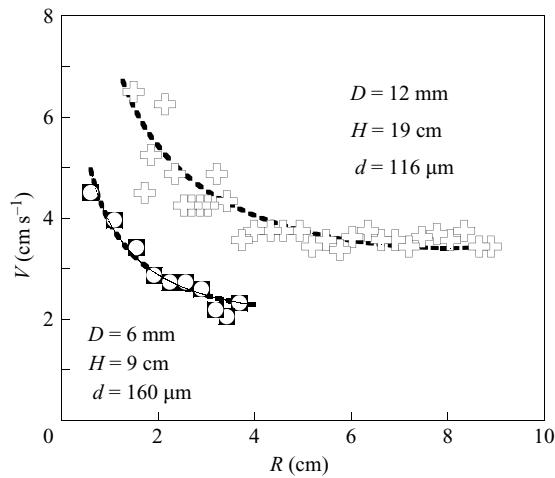

FIGURE 12. A typical variation of the closing speed of the jump versus the radial distance R. The solid line is the result of (5.4) given in the text.

characteristics, its speed and its height, are correctly described using the momentum flux/pressure balance.

It should be noted here that this height profile ends with a sharp cutoff at a well-defined position R_J which is different from the stopping distance R_M discussed above. This observation will be explained below.

6. Transient regime and the initial granular jump

The initial stopping of the horizontal layer involves a transient regime, whose behaviour presents some differences from the stationary regime. A sequence of images as the jet first hits the surface is shown in figure 13. The differences between the transient and stationary regimes are already apparent in the vertically falling jet whose first front, more exposed to the air friction, is slower and locally enlarged, as seen in the first two photographs of figure 13. As the bottom part of the jet hits the surface, it expands radially outwards as seen 24 ms later. This first front becomes ring-like as it travels farther from the impact point as seen 48 ms after. This ring grows in importance as it continues to expand, as shown for 80 ms and later times.
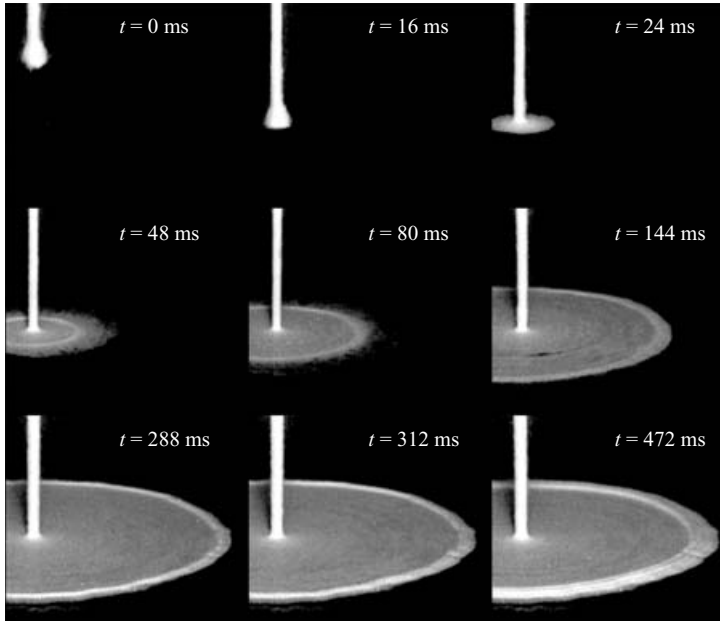
FIGURE 13. Transient regime. A sequence of images showing the first stages of the experiment when the jet first impacts the surface. The following stages show how the sand spreads out and stops at a well-defined position away from the impact. Once this stopping occurs, a sand front starts to advance towards the impact point.

In this sequence of images, we can therefore follow the initial stages of formation of the initial jump very accurately. The velocity of the first ring turns out to be smaller than the velocity V_0 determined in the stationary regime so the arrest point of this first ring occurs at a radius R_J smaller than the position R_M. Typically, the ratio R_J/R_M varies between 0.8 and 0.9. Once the first ring stops at R_J, which occurs in the example shown in figure 13 at $t = 312$ ms, the continuous flow in the horizontal layer starts to accumulate at this point, and the sand front starts its advance towards the injection point as shown for $t = 472$ ms. At later times, the stationary regime is well established. The cutoff observed for the profile displayed previously occurs at R_J; the height of the pile at this point will be denoted h_J and examined below. As a result, the profile $h_c(R)$ matches continuously with the initial jump at $R = R_J$, $h_c(R_J) = h_J$ and its height increases for $R < R_J$. The region $R > R_J$ is screened by the initial jump formed by the first propagating ring. The profile $h_c(R)$ has, here, a sharp cutoff as seen previously, in such a way that the jump height h_J and the jump radius R_J can be measured by inspection of $h_c(R)$ near its endpoint.

We thus reduce, within a good approximation, the complicated dynamics of the flow arrest to the following picture. After the arrest of the first propagating ring at $R \approx R_J$, the remaining part of the flow concentrates its deposition around this point as long as its height is below h_J. This stage corresponds to the initial granular jump formation. Then the remaining part of the flow collides with the initial jump and its deposition appears as a sand front which moves towards the injection centre.

6.1. *Determination of the initial jump radius and height*

In §4.3, we have studied the horizontal layer in its stationary regime. We recall that this flow leaves the impact region at $R = R_0$ with a speed V_0 given in (4.6),
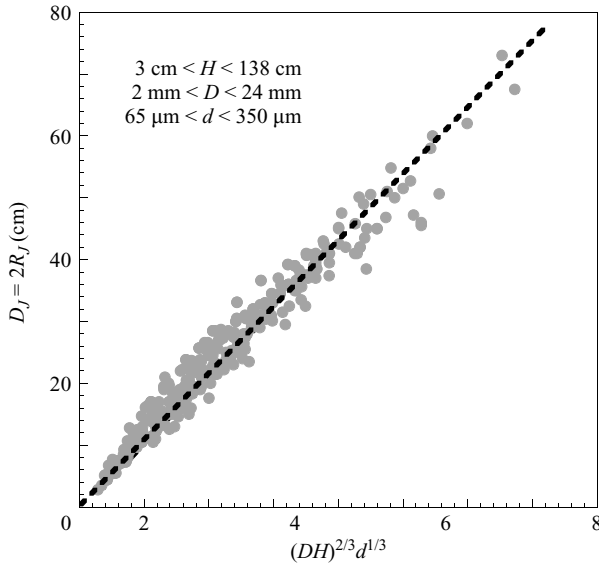
FIGURE 14. The initial jump diameter $D_J = 2R_J$ as a function of $(HD)^{2/3}d^{1/3}$ for different chute heights, funnel diameters and bead diameters.

decelerates according to the Coulomb law and would stop at $R_M = V_0^2/2\mu g$. We have studied the transient regime as the jet first hits the surface and here we summarize our observations. The corresponding impact region becomes progressively denser and smoother. However, R_0 cannot be identified as easily as in the stationary regime. Nonetheless, the first front of the horizontal layer behaves qualitatively as in the stationary regime: it is subject to the same Coulomb deceleration, but its speed V_I at $R = R_0$ is always lower than V_0. This is because for the first front produced after the jet first hits the surface, the vertical chute speed and the restitution factor of the impact region are smaller than for the stationary regime. The ratio V_I/V_0 appears to be independent of the chute height and depends very weakly on D and d. Thus, $R_J = V_I^2/2\mu g < R_M$ (the point R_M is never reached as already explained). The measurements of R_J are summarized in figure 14. This arrest distance turns out to depend on H, D and d and the best rescaling we could find is shown in figure 14 where R_J is plotted versus $(HD)^{2/3}d^{1/3}$. In order to appreciate this point further, we plot in figure 15, $V_0(R)$ measured in the stationary regime and the velocity of the first ring $V_r(R)$. The velocity of the first ring is always smaller than the velocity of the horizontal layer at all values of R. The velocity of the first ring also vanishes at a smaller distance than $V_0(R)$. The most surprising aspect of these measurements is that the friction coefficient for the first ring turns out to be smaller than the coefficient determined for the stationary flow of the horizontal layer. The measured value for the first ring is about 0.3 (the mean value from a set of measurements is 0.3 ± 0.05) whereas we had measured 0.6 for the stationary regime. We do not know what the origin of this difference is. The first ring seems to be compact while the horizontal layer is dilute, so this difference seems surprising as it would indicate a higher friction coefficient for the more dilute flow. The value of 0.3 measured for the first ring is slightly lower than the dynamic friction coefficient for glass on glass (0.4) while the more dilute flow shows a higher value.

The initial jump height h_J is given by the height of the sand-pile profile at $R = R_J$. This height increases linearly with the funnel diameter D (figure 16). This height also
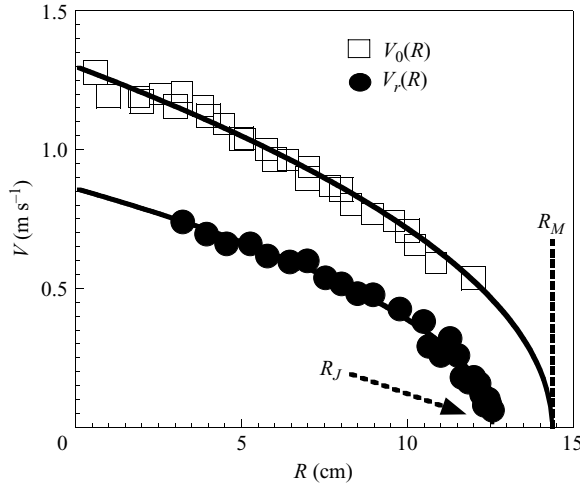
FIGURE 15. A comparison between the velocity of the horizontal layer versus the radial distance in the stationary regime and the velocity of the first ring (transient regime) versus the radial distance. Both curves are fit to predictions based on Coulomb friction giving values of the friction coefficient of 0.6 and 0.3, respectively.
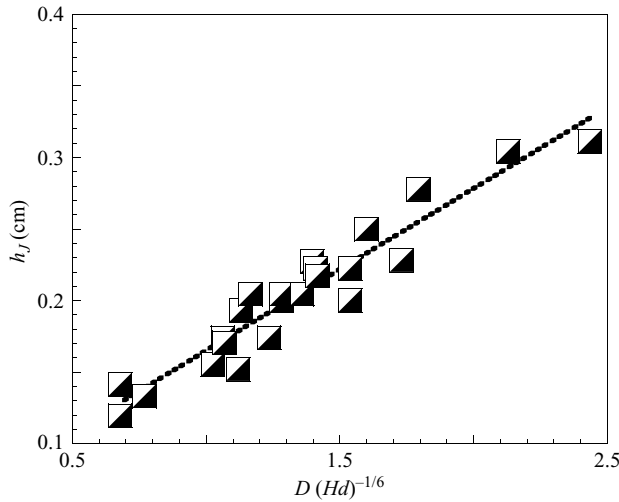

FIGURE 16. The variation of h_J as a function of $D(Hd)^{-1/6}$.

depends very weakly on H and d. Considering the scaling found for R_J and the shape of the profile $h_c(R)$, h_J is expected to scale as $D(Hd)^{-1/6}$ which is borne out experimentally. The observed dependence of R_J and h_J on the parameters H, D and d calls for an extra length scale. Indeed, to write the observed scalings correctly so that both R_J and h_J scale as a length, we must introduce a characteristic length scale l_0. The scalings then read: $R_J = l_0^{-2/3}(HD)^{2/3}d^{1/3}$ and $h_J \sim l_0^{1/3}D(Hd)^{-1/6}$. From fits to the varitation of R_J and h_J, the value of l_0 turns out to be 0.8 mm. This length is therefore of order 1 mm. We do not know at present what the meaning of this extra length scale is, considering that the other length scales of the problem have all been used. All we can say is that this length scale is associated with the transient state of the impact of the jet on the solid surface.
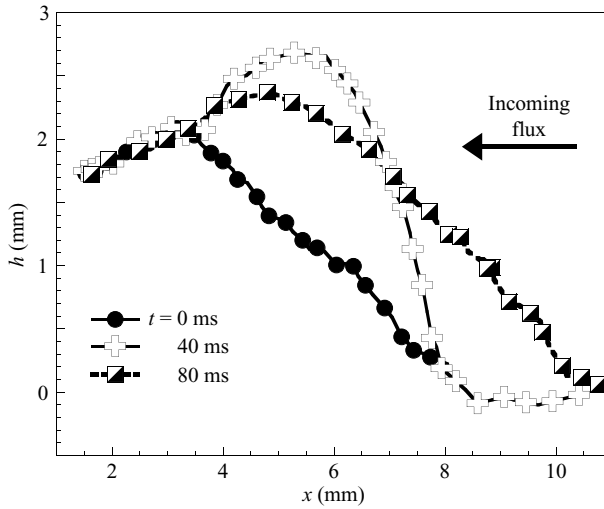
FIGURE 17. The dynamics of the moving sand front: during one cycle, the sand front angle starts out small, increases to high values by deposition, before becoming small again by avalanching at the end of the cycle. The cycle here lasts 80 ms.
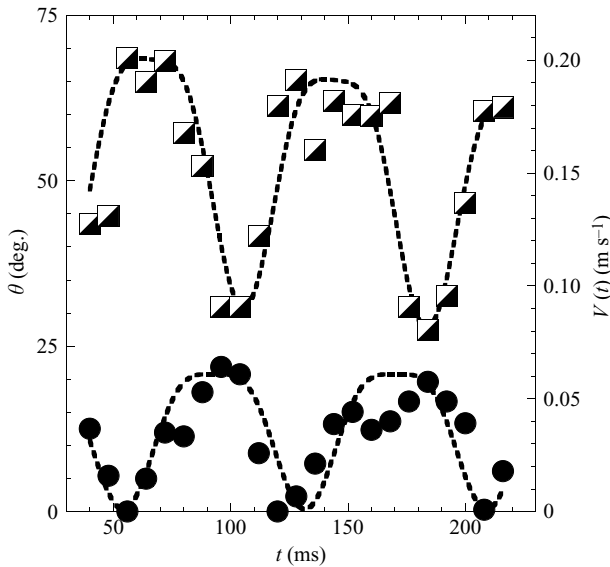

FIGURE 18. The variations of the front angle and the velocity of the base of the front during several oscillations. Note that the angle oscillates between angles close to the repose angle and angles as high as 70°. The velocity of the base oscillates also and goes through periods (for which the angle is small) where it is basically zero indicating a pinning of the base while the angle of the front increases.

6.2. *Relation between the transient phase and the filling phase at small scale*

For completeness, we now consider the sand pile as it advances towards the origin once the initial jump is built, but our aim is to describe the small-scale details of the front dynamics. As shown in figures 17 and 18, the advancing front has an oscillating dynamic. A front profile is shown in figure 17 for three different times corresponding

to one cycle of the oscillating dynamics of the front. The front starts out with a small angle and owing to deposition of the incoming sand, the front angle increases as shown for 40 ms later. As the front reaches high angles, the angle decreases by avalanching to reach a state (80 ms later) similar to the first profile with a smaller front angle. Figure 18 illustrates these oscillations. The velocity of the base oscillates as in stick–slip motion while the average angle of the front oscillates between a small angle close to the angle of repose and a high angle which can reach over 60°. The horizontal flow collides with the grains previously accumulated and this induces instabilities of the front. The instability of the front stems from the difference between R_M and R_J and therefore to the presence of the transient state described above. Once the initial front stops at R_J, the incoming flux which should stop at R_M, climbs up the initial jump. This climbing increases the slope at the front. If this slope becomes sufficiently strong, avalanches would ensue. This avalanching would then continue since, at any instant, the front is at a shorter distance than the true arrest point and the velocity of the incoming grains is sufficient for climbing up the slope. This simple argument can be made more quantitative by considering the energy balance at the front. The wavelength of the pattern is of order h_J and the maximal angle is related to the minimal angle of the front by a simple relation $\tan\theta_M \approx 4\tan\theta_m$. The experimental details of the front dynamics have been reported in (Boudet *et al.* 2005) and the semiquantitative analysis of these dynamics will be reported elsewhere.

7. Conclusion

Through a detailed study of the impact of a jet of granular material on a smooth solid surface, we have analysed the properties of the falling jet, the impact zone, the fast flow of the material following this impact, and the formation of the jump itself. The thinning of the jet during its fall, the fast radial flow, and the existence of the jump are shared by both granular materials and liquids. The thinning of the jet is found to obey a universal scaling law. The impact region turns out to have a universal character as well. The jump here advances towards the jet impact position, unlike for liquids where it is static. Still, a balance between momentum flux across the jump and the difference in pressure across it can be used to understand the velocity of the front as well as the height of the jump. This also allows us to predict the shape of the final sand pile. However, the presence of compressibility and therefore variations of density play an important role and have to be taken into account explicitly. Other features and in particular the presence of small-scale oscillatory dynamics are directly related to the granular nature of the medium. The front is unstable towards oscillations of its front angle and speed owing to the presence of avalanches (a granular feature). The granular jump studied here therefore brings forth the interplay between continuum hydrodynamic properties and the granular and discrete nature of the medium.

REFERENCES

AMAROUCHENE, Y. & KELLAY, H. 2006 Speed of sound from shock fronts in granular flows. *Phys. Fluids* **18**, 031707.

AMAROUCHENE, Y., BOUDET, J. F. & KELLAY, H. 2001 Dynamic sand dunes. *Phys. Rev. Lett.* **86**, 4286.

BONNIER, B., BOUDET, J.-F. & KELLAY, H. 2003 Granular flow trapped on an incline: dynamics of the sand pile. *Phys. Rev.* E **68**, 061302.

BOUCHAUD, J. P., CATES, M. E., RAVI PRAKASH, J. & EDWARDS, S. F. 1994 A model for the dynamics of sand pile surfaces. *J. Phys.* I **4**, 1383.

BOUDET, J-F., GAUTHIER, S., AMAROUCHENE, Y. & KELLAY, H. 2003 Self-similar dynamic quasi-two-dimensional sand fronts. *Phys. Rev.* E **67**, 010303(R).

BOUDET, J. F., AMAROUCHENE, Y., BONNIER, B. & KELLAY, H. 2005 Non-aeolian sand ripples. *Europhys. Lett.* **69**, 365.

BUSH, J. W. M. & ARISTOFF, J. M. 2003 The influence of surface tension on the circular hydraulic jump. *J. Fluid Mech.* **489**, 229.

CONWAY, S. L., SHINBROT, T. & GLASSER, J. 2004 A Taylor vortex analogy in granular flows. *Nature* **431**, 433.

DURAN, J. 1997 Sables *Poudres et Grains*. Eyrolles Sciences, Paris.

GARCIMARTIN, A., MAZA, D., ILQUIMICHE, J. L. & ZURIGUEL, I. 2002 Convective motion in a vibrated granular layer. *Phys. Rev.* E **65**, 031303.

DE GENNES, P. G. 1999 Granular matter: a tentative view. *Rev. Mod. Phys.* **71**, 374.

GOLDFARB, D., GLASSER, B. J. & SHINBROT, T. 2002 Shear instabilites in a granular flow. *Nature* **415**, 302.

GRAY, J. M. N. T., TAI, Y.-C. & NOELLE, S. 2003 Shock waves, dead zones and particle-free regions in rapid granular free-surface flows. *J. Fluid Mech.* **491**, 161.

HÁKONARDÓTTIR, K. M. & HOGG, A. J. 2005 Oblique shocks in rapid granular flows. *Phys. Fluids* **17**, 077101.

JAEGER, M., NAGEL, S. R. & BEHRINGER, R. P. 1996 Granular solids, liquids, and gases. *Rev. Mod. Phys.* **68**, 1259.

KADANOFF, L. P. 1999 Built upon sand: theoretical ideas inspired by granular flows. *Rev. Mod. Phys.* **71**, 435.

LIU, A. J. & NAGEL, S. R. 1998 Jamming is not just cool anymore. *Nature* **396**, 21–22.

MAHADEVAN, L. & POMEAU, Y. 1999 Propagating fronts on sand pile surfaces. *Europhys. Lett.* **46**, 595.

MELO, F., UMBANHOWAR, P. & SWINNEY, H. L. 1995 Hexagons, kinks, and disorder in oscillated granular layers. *Phys. Rev. Lett.* **75**, 3838–3841.

MIDDLEMAN, S. 1995 *Modeling Axisymetric Flows*. Academic.

NAGEL, S. R. 1992 Instabilities in a sand pile. *Rev. Mod. Phys.* **64**, 321.

NICOLAS, M. 2002 Experimental study of gravity-driven dense suspension jets. *Phys. Fluids.* **14**, 3570.

POULIQUEN, O. & FORTERRE, Y. 2002 Friction law for dense granular flows: application to the motion of a mass down a rough inclined plane. *J. Fluid Mech.* **453**, 133–151.

RERICHA, E., BIZON, C., SHATTUCK, M. D. & SWINNEY, H. L. 2002 Shocks in supersonic sand. *Phys. Rev. Lett.* **88**, 014302.

SAVAGE, S. B. & HUTTER, K. 1989 The motion of a finite mass of granular material down a rough incline. *J. Fluid Mech.* **199**, 177–215.

STARON, L. & HINCH, E. J. 2005 Study of the collapse of granular columns using two dimensional discrete-grain simulation. *J. Fluid Mech.* **545**, 1.

WATSON, E. J. 1964 The spread of a liquid jet over a horizontal plane. *J. Fluid Mech.* **20**, 481.

ZURIGUEL, I., BOUDET, J. F., AMAROUCHENE, Y. & KELLAY, H. 2005 Role of fluctuation-induced interactions in the axial segregation of granular materials. *Phys. Rev. Lett.* **95**, 258002.